CHEMISTRY

Self-supported hydrogenolysis of aromatic ethers to arenes

Qinglei Meng[1]*, Jiang Yan[1,2], Huizhen Liu[1,2,3], Chunjun Chen[1,2], Shaopeng Li[1,2], Xiaojun Shen[1,2], Jinliang Song[1], Lirong Zheng[4], Buxing Han[1,2,3,4]*

Arenes are widely used chemicals and essential components in liquid fuels, which are currently produced from fossil feedstocks. Here, we proposed the self-supported hydrogenolysis (SSH) of aromatic ethers to produce arenes using the hydrogen source within the reactants, and it was found that RuW alloy nanoparticles were very efficient catalyst for the reactions. This route is very attractive and distinguished from the reported studies on the cleavage of the C_{Ar}—O bonds. The unique feature of this methodology is that exogenous hydrogen or other reductant is not required, and hydrogenation of aromatic rings could be avoided completely. The selectivities to arenes could reach >99.9% at complete conversion of the ethers. Moreover, lignin could also be transformed into arenes efficiently over the RuW alloy catalyst. The mechanism studies showed that the neighboring Ru and W species in the RuW alloy nanoparticles worked synergistically to accelerate the SSH reaction.

INTRODUCTION

Utilization of biomass as raw materials to produce useful chemicals and fuels can liberate us from the reliance on fossil resources and can also be considered as recycling of CO_2 by combination of photosynthesis and chemical methods (1, 2). With the robust aryl carbon—oxygen bond (C_{Ar}—O) built and functionalized, aromatic ethers are ubiquitous in the natural world (3). Lignin, a major component of lignocellulosic biomass, is the most abundant aromatic ether in nature and is thus the most obvious and promising renewable source of the aromatic building blocks on which the chemical industry can heavily rely (4–6). Besides, small-molecule aromatic ethers, such as methoxytoluene/dimethoxytoluene (7, 8), di-/trimethoxybenzene (9, 10), methyleugenol (11), and asarone (12), also existed in various plants but with far less quantities than lignin. With a benzene ring as its main structural characteristic, biomass-derived aromatic ethers can be potentially used to produce industrially relevant aromatic bulk and fine chemicals (13), which are currently obtained from fossil resources (14, 15). However, the highly complex molecular structure of the aromatic ethers, combined with their highly recalcitrant and stable chemical natures, has so far hampered many efforts to increase their values (16). Although different transformation methods, such as hydrogenation reduction (17–19), oxidation (20–22), hydrolysis/acidolysis (23, 24), and cross-coupling (25, 26), have produced encouraging results, their products have still been widely distributed and overfunctionalized. Currently, a very limited number of high-purity industrial chemicals can be obtained from the aromatic ethers, especially from lignin, which has a high molecular weight and is rich in C_{Ar}—O bonds with high energies and low reactivities (27–29).

By experience, hydrodeoxygenation (HDO), which has been proved efficient in the cleavage of C_{Ar}—O bonds with hydrogen present, should be the convenient and feasible pathway to convert biomass to commodity chemicals with narrow distribution, such as aromatic hydrocarbons, which can be industrially used as the industrial raw materials (30) and transport fuels (31). However, in the conventional HDO reactions, the concomitant hydrogenation of the aromatic ring cannot be avoided completely (17, 32), although high selectively can be reached (Fig. 1A). Lee et al. (33) conducted vapor-phase HDO of anisole over Mo_2C catalysts at lower temperatures and ambient hydrogen pressure, which made a remarkable progress in traditional HDO, giving benzene selectivity more than 90%. Besides, transition-metal complexes combined with equivalent strong hydride reductant, such as 1,1,3,3-tetramethyldisiloxane, could also efficiently catalyze the cleavage of C_{Ar}—O bonds, with high aromaticity retained. However, this route required expensive reductant, and air and water-free conditions, which weaken the industrial feasibility (34). There exist some challenges in C_{Ar}—O bond cleavage chemistry, such as realization of full aromaticity production without saturation of the aromatic ring, establishment of atom-economical and feasible strategies (35), and achievement of high aromaticity in the transformation of complex reactants. In this regard, much effort is still needed to develop novel strategies, which is crucial for designing many previously unidentified catalytic reactions (3) and is also a key step in the valorization of biomass resources.

Here, we report the work on self-supported hydrogenolysis (SSH) strategy for the transformation of C_{Ar}—O bonds in aromatic ethers to produce arene as the single product (Fig. 1B). It was found that different aromatic ethers including lignin could be transformed into arenes over the highly efficient RuW alloy catalyst without any exogenous hydrogen or other reductant input, and the selectivity could be >99.9% (no by-product could be detected). The unique feature of this methodology is that the hydrogen within the reactants is used as the hydrogen source, and the exogenous hydrogen or other reductant is not required in the SSH reaction. Moreover, the side reaction, such as hydrogenation of the aromatic ring, can be avoided completely. As far as we know, there is no related report with regard to the SSH chemistry.

[1]Beijing National Laboratory for Molecular Sciences, CAS Laboratory of Colloid and Interface and Thermodynamics, CAS Research/Education Center for Excellence in Molecular Sciences, Institute of Chemistry, Chinese Academy of Sciences, Beijing 100190, China. [2]School of Chemistry and Chemical Engineering, University of Chinese Academy of Sciences, Beijing 100049, China. [3]Physical Science Laboratory, Huairou National Comprehensive Science Center, No. 5 Yanqi East Second Street, Beijing 101400, China. [4]Institute of High Energy Physics, Chinese Academy of Sciences, Beijing 100049, China.
*Corresponding author. Email: mengqinglei@iccas.ac.cn (Q.M.); hanbx@iccas.ac.cn (B.H.)
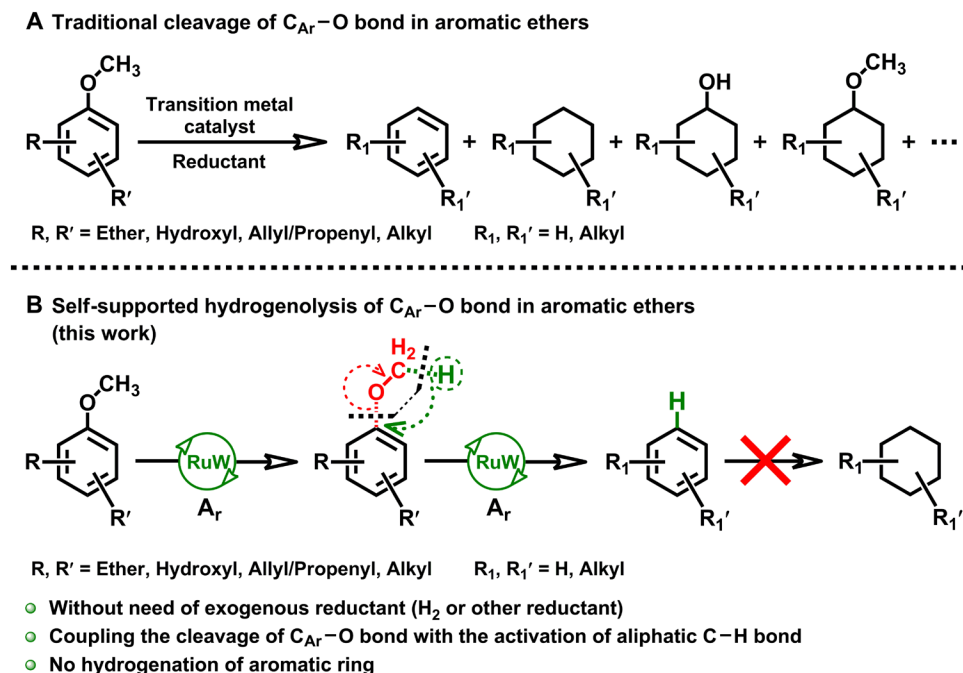
Fig. 1. Strategies used for the transformation of aromatic ethers.
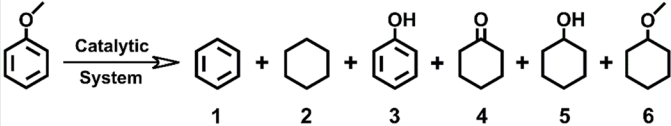
RESULTS

We used anisole to screen the catalytic system for SSH reaction of aromatic ethers because it has only one methoxy group ($O-CH_3$) that simplifies the experimental study. Table 1 presents the results of the anisole transformation under different conditions using various catalysts. As expected, the conversion of anisole did not occur without the catalyst or when only SiO_2 (fig. S1) was used (Table 1, entry 1). Monometallic catalysts, such as Ru, Pt, Pd, and Ni, were also prepared and used (Table 1, entries 2 to 5) because they are commonly used catalysts for hydrogenation and hydrogenolysis reactions (25, 36, 37). However, anisole was completely unreactive under Ar atmosphere over the above monometallic catalysts. It has been reported that tungsten (W) usually serves as a promoter in a bifunctional catalyst, which is more effective in cleavage of the $C_{Ar}-O$ bond than the corresponding monometallic counterparts (38). In an attempt to yield benzene from anisole via the SSH method, a series of W-containing bimetallic catalysts were prepared and their catalytic performances for promoting the reaction were studied (Table 1, entries 6 to 9). It can be found that the selectivity to benzene could be >99.9% at 96.9% conversion of anisole over the RuW/SiO_2 catalyst under Ar atmosphere in 4.5 hours (Table 1, entry 6, and fig. S2A), and according to the ^{1}H nuclear magnetic resonance (NMR) analysis of the aqueous phase (fig. S2B), there was no water-soluble product. Hydrogen and CO_2 were the main gaseous products (fig. S2C). The anisole could be completely converted in 5 hours with a turnover number of 38, and the selectivity remained to be >99.9% (Table 1, entry 7). The catalytic activities and selectivities of benzene were both much lower over PtW/SiO_2 and PdW/SiO_2 catalysts (Table 1, entries 8 and 9). When the NiW/SiO_2 catalyst was used, the reaction did not occur under the same conditions (Table 1, entry 10). In addition, the conversion of anisole over the mechanical mixture of the Ru/SiO_2 and W/SiO_2 catalyst (Ru-W/SiO_2; Table 1, entry 11) was much lower than that over the RuW/SiO_2 catalyst

(Table 1, entry 7), although the selectivity of benzene was also very high, indicating that the Ru and W components in the catalyst mixture did not cooperate well.

For comparison, the transformation of anisole over the bimetallic catalysts was also studied under H_2 atmosphere. Significant hydrogenation of the benzene ring occurred during the reactions over all the above catalysts at different anisole conversions (Table 1, entries 12 to 15). Moreover, the benzene ring was hydrogenated completely over the monometallic Ru/SiO_2 catalyst, and cyclohexane and methoxycyclohexane were generated under similar anisole conversion (Table 1, entry 16). The results indicate that the above bimetallic and monometallic catalysts were all prone to hydrogenating the aromatic ring with exogenous hydrogen in both the traditional HDO or hydrogenolysis deoxygenation route. Nevertheless, anisole was completely unreactive under Ar or H_2 atmosphere over the monometallic W/SiO_2 catalyst (Table 1, entries 17 and 18). Moreover, the transformation of anisole was also studied in different solvent systems (table S1). The results indicated that water was the best among the tested solvents for the SSH reaction. One of the reasons may be that water can form hydrogen bonds with the O atom in anisole, which was beneficial for the SSH reaction (39). The solvent effect is very interesting but needs to be studied further. In addition, it is known that the solubility of a hydrophobic compound in water increases with increasing temperature (40). Thus, at our experimental temperature, the solubility of anisole in water is high enough for efficient reaction.

According to the control experiments summarized in Table 1, monometallic catalysts were not active for the transformation of anisole without exogenous hydrogen (Table 1, entries 2 to 5 and 17), whereas anisole could be converted into benzene selectively and efficiently over the bimetallic RuW catalyst (Table 1, entries 6 and 7), indicating that both Ru and W components were necessary for the reaction, and they cooperated very well for the SSH reaction.

Table 1. Results for the transformation of anisole over supported metal catalysts at different conditions.

| Entry | Catalytic system* | | T (hours) | Conversion (%) | Selectivity (%) | | | | | | Yield of 1 (%) |
	Catalyst†	Gas			1	2	3	4	5	6	
1‡	–	Ar	4.5	0.0	0.0	0.0	0.0	0.0	0.0	0.0	0.0
2	Ru/SiO₂	Ar	4.5	0.0	0.0	0.0	0.0	0.0	0.0	0.0	0.0
3	Pt/SiO₂	Ar	4.5	0.0	0.0	0.0	0.0	0.0	0.0	0.0	0.0
4	Pd/SiO₂	Ar	4.5	0.0	0.0	0.0	0.0	0.0	0.0	0.0	0.0
5	Ni/SiO₂	Ar	4.5	0.0	0.0	0.0	0.0	0.0	0.0	0.0	0.0
6	RuW/SiO₂	Ar	4.5	96.6	>99.9	0.0	0.0	0.0	0.0	0.0	96.5
7§	RuW/SiO₂	Ar	5.0	100	>99.9	0.0	0.0	0.0	0.0	0.0	>99.9
8	PtW/SiO₂	Ar	4.5	28.8	80.2	0.0	19.8	0.0	0.0	0.0	23.1
9	PdW/SiO₂	Ar	4.5	20.5	73.7	0.0	17.0	9.3	0.0	0.0	15.1
10	NiW/SiO₂	Ar	4.5	0.0	0.0	0.0	0.0	0.0	0.0	0.0	0.0
11‖	Ru-W/SiO₂	Ar	5.0	9.8	>99.9	0.0	0.0	0.0	0.0	0.0	9.8
12	RuW/SiO₂	H₂	4.5	96.5	78.8	21.2	0.0	0.0	0.0	0.0	76.0
13	PtW/SiO₂	H₂	4.5	96.8	11.8	31.2	0.0	3.2	19.5	34.3	11.8
14	NiW/SiO₂	H₂	4.5	25.6	31.8	18.2	0.0	9.1	15.5	25.4	8.1
15	PdW/SiO₂	H₂	4.5	97.0	0.0	67.7	0.0	0.5	21.1	10.7	0.0
16	Ru/SiO₂	H₂	1.0	95.9	0.0	42.0	0.0	0.0	4.6	53.4	0.0
17	W/SiO₂	Ar	4.5	0.0	0.0	0.0	0.0	0.0	0.0	0.0	0.0
18	W/SiO₂	H₂	4.5	0.0	0.0	0.0	0.0	0.0	0.0	0.0	0.0

*Reaction results are the averages of three experiments conducted in parallel. Anisole (1.0 mmol), H_2O (5.0 ml), 175°C, 0.5 MPa Ar, or 1.0 MPa H_2, 800 rpm. †Ru/SiO₂ (3.5 wt %), Pt/SiO₂, Pd/SiO₂, Ni/SiO₂, 20 wt % W/SiO₂ (the content of metal is based on SiO₂ and determined by ICP); RuW/SiO₂, PtW/SiO₂, PdW/SiO₂, NiW/SiO₂ (3.5 wt % Ru, Pt, Pd, and Ni metals, 20 wt % W, the content of metal is based on SiO₂ and determined by ICP). ‡Without catalyst, or only SiO₂ was used. §Turnover number (TON) = 38; TON is expressed in mole of anisole converted per mole of ruthenium. ‖Mechanical mixture of Ru/SiO₂ (3.5 wt % Ru) and W/SiO₂ (20 wt % W) catalysts is denoted as Ru-W/SiO₂ catalyst.

Therefore, to get insight into the cooperation of Ru and W species, we conducted systematic characterizations of the RuW/SiO₂ catalyst. A typical x-ray diffraction (XRD) pattern of the as-synthesized RuW/SiO₂ is presented in Fig. 2A. As compared with the standard pattern of RuW alloy, the positions of the diffraction peaks of the RuW/SiO₂ catalyst were well defined, indicating the alloy structure of the RuW nanoparticles (NPs), rather than mixed phases of Ru and W species. Figure 2B shows the transmission electron microscopy (TEM) images of the RuW NPs supported on the amorphous SiO₂ (fig. S1). The RuW NPs were well dispersed with particle size in the range of 1.0 to 4.0 nm. The high-resolution TEM (HRTEM) image of the RuW NPs in Fig. 2C shows a lattice fringe spacing of 0.208 nm. The catalyst was further characterized by elemental mapping and linear scan energy-dispersive x-ray spectroscopy (EDS). The elemental mapping gives a direct view of the homogeneous distribution of Ru and W atoms in each NP (fig. S3, A to C). The EDS line scan across a RuW alloy NP with a particle size of 3.5 nm (Fig. 2C) also demonstrates that Ru and W atoms are well alloyed, as shown in Fig. 2D. Moreover, the electronic structure of the Ru and W species was characterized by x-ray photoelectron spectroscopy (XPS). The XPS peaks that appeared at 461.76 eV (Fig. 2E) and 31.91 eV (Fig. 2F) correspond to the metallic Ru 3p and W 4f orbitals of the Ru and W species in the RuW/SiO₂ catalyst (41). Evidently, the Ru 3p binding energy in the RuW/SiO₂ catalyst showed a negative shift compared to Ru/SiO₂ (Fig. 2E). Meanwhile, an opposite tendency was observed for the W 4f orbital peak, which shifted to higher binding energy than that of the W/SiO₂ catalyst. It should be ascribed to the higher electronegativity of Ru that results in the electron transfer from W to Ru, indicating the well-alloyed structure of Ru and W species in the RuW/SiO₂ catalyst (42). To further study the crystal structure of RuW alloy NPs and confirm the atomic site assignment, the Rietveld refinement analysis was carried out using XRD data of the as-synthesized RuW/SiO₂ catalyst (Fig. 2G). The refinement revealed that the RuW alloy was the only crystal phase and the random occupancies of Ru and W atoms in the crystal structure are estimated to be 20.4 and 79.6%, which basically correspond to the reference RuW alloy (Fig. 2A). To further identify the structure of the RuW alloy, we also conducted x-ray absorption
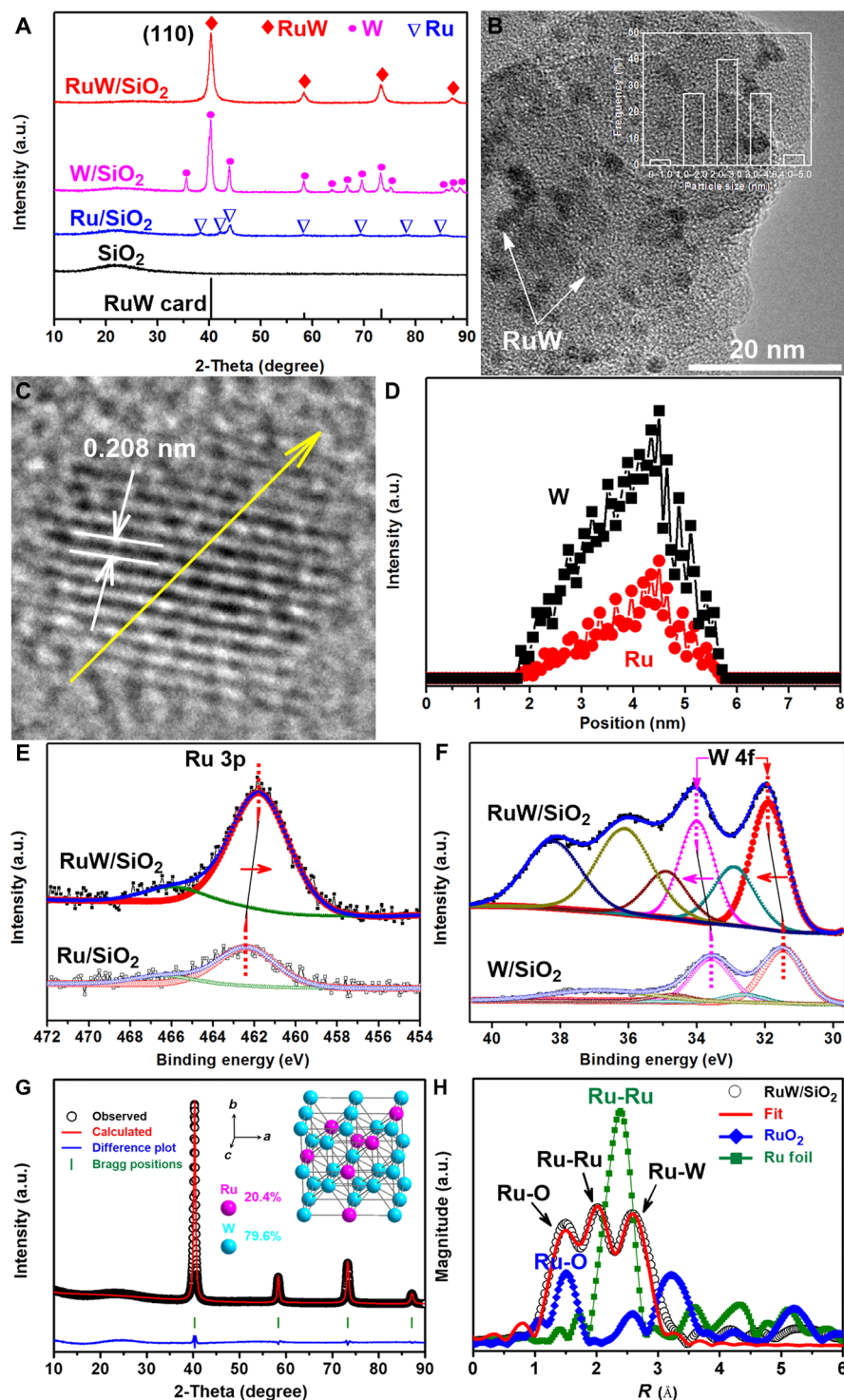
Fig. 2. Characterization of RuW/SiO$_2$ catalyst. (**A**) XRD patterns of RuW/SiO$_2$ [3.5 weight % (wt %) Ru, 20 wt % W] catalyst (red), W/SiO$_2$ (20 wt % W) catalyst (pink), Ru/SiO$_2$ (3.5 wt % Ru) catalyst (blue), and amorphous SiO$_2$ (black). Standard pattern of RuW alloy from [International Centre For Diffraction Data Portable Document Format (ICDD PDF)] card (65-6705 for RuW) is shown at the bottom. (**B**) TEM image of RuW/SiO$_2$ catalyst (inset: RuW alloy particle size distribution of RuW/SiO$_2$ catalyst). (**C**) HRTEM image of RuW/SiO$_2$ catalyst. (**D**) HRTEM EDS line scan profiles of W (black) and Ru (red) in the RuW/SiO$_2$ catalyst recorded along the arrow shown in the HRTEM image (C), XPS spectra for Ru 3p region (**E**), and W 4f region (**F**). (**G**) Rietveld refinement of RuW/SiO$_2$ catalyst (3.5 wt % Ru, 20 wt % W) using XRD pattern in (A) (inset: crystal structure of RuW alloy NPs). White circle marks (○) represent the observed intensities, and the red solid line is Rietveld-fit profile. The difference plot (blue) is shown at the bottom. The olive tick marks indicate the positions of the Bragg reflections as obtained in the Rietveld refinement. The RuW alloy parameters are as follows: space group Im-$3m$, $a = b = c = 3.1609$ Å. $R_p = 7.60\%$ and $R_{wp} = 9.32\%$. (**H**) Fourier-transformed (FT) EXAFS k^2-weighted $\chi(k)$ function spectra of RuW/SiO$_2$ (3.5 wt % Ru, 20 wt % W) catalyst, references, and corresponding EXAFS R-space fitting curve for RuW/SiO$_2$.

near-edge structure (XANES) and extended x-ray absorption fine structure (EXAFS) characterizations. The Ru K-edge XANES curves (fig. S4A) showed that the energy absorption threshold value is slightly lower than that of the Ru foil, which was consistent with XPS data (Fig. 2E), despite the fact that the shift tendency to higher threshold value was inconspicuous for W L_3-edge (fig. S4B). The corresponding Fourier-transformed EXAFS curves (Fig. 2H and fig. S4C) exhibited main peaks associated with Ru-Ru, Ru-W, and W-W scatterings (43, 44). Quantitative EXAFS curve fitting was also carried out, and the corresponding fitting parameters are listed in table S2. The coordination number of Ru-W was 3.2, and its corresponding mean bond length was 2.88 Å, proving that Ru and W atoms were alloyed in the RuW/SiO$_2$ catalyst. The local coordination essentially fit the expected bimetallic RuW alloy formation. The W-Ru scatterings were not observed, which should be due to the high W/Ru molar ratio in the catalyst (fig. S4C).

Density functional theory (DFT) studies were performed to get more insight into the mechanism of the SSH reaction over the RuW catalyst. The calculated energy profile is shown in Fig. 3 and fig. S5, and the detailed optimized geometry structures are summarized in fig. S5B. Two main reaction pathways for the SSH reaction of anisole to benzene were considered in our calculations: In path I, the aliphatic C—H (C$_{Al}$—H) bond is first activated to produce a *C$_6$H$_5$OCH$_2$+*H intermediate (IM1a, Fig. 3) followed by the hydrogenolysis of the C$_{Ar}$—O bond in *C$_6$H$_5$OCH$_2$ to generate benzene and formaldehyde (path I, inset in Fig. 3, green dashed lines). Path II involves initial cleavage of the C$_{Ar}$—O bond to a *C$_6$H$_5$+*OCH$_3$ intermediate (IM1b, fig. S5A) followed by the activation and dissociation

of the C$_{Al}$—H bond in *OCH$_3$ to formaldehyde and benzene (path II, inset in Fig. 3, red dashed lines). As shown in Fig. 3, the energy barriers for the dissociation of the C$_{Al}$—H bond in paths I and II are 0.31 and 0.29 eV, respectively. The barriers for cleavage of the C$_{Ar}$—O bond in paths I and II are 0.59 and 0.87 eV, respectively. Thus, the rate-determining step of the SSH reaction on the RuW catalyst is the cleavage of the C$_{Ar}$—O bond in both paths. It can be known from the results that SSH of anisole preferred path I because the energy barrier for the rate-determining step of this path (0.59 eV) was much lower than that of path II (0.87 eV). The generation of formaldehyde was proved from the SSH of anisole (fig. S6A), further supporting the pathway. However, during the reaction at 175°C, the generated formaldehyde decomposed into hydrogen and CO$_2$ as the main products (45), which could be observed in the gas chromatography (GC) traces of the gaseous sample (fig. S2C). In addition, an isotope labeling test of anisole-(methyl-d3) (PhOCD$_3$) in H$_2$O was conducted (fig. S6B), and the molecular weight of benzene was shown as 79, confirming that the hydrogen in the SSH reaction was from the methoxy group, rather than the water. Moreover, the molecular weight was 78 when the transformation of anisole was performed in deuterium oxide (D$_2$O) (fig. S6C), which again proved that D in D$_2$O was not incorporated in the benzene. This further indicates that the hydrogenolysis of the C$_{Ar}$—O bond proceeded with the negatively charged hydrogen (fig. S6D) from the C$_{Al}$—H bond in path I (Fig. 3), but not with the water-derived H proton.

The above reaction mechanism is further supported by the transformation of phenol (table S3, entry 1), and other substrates in which the hydrogen atoms in the methoxy group of anisole are
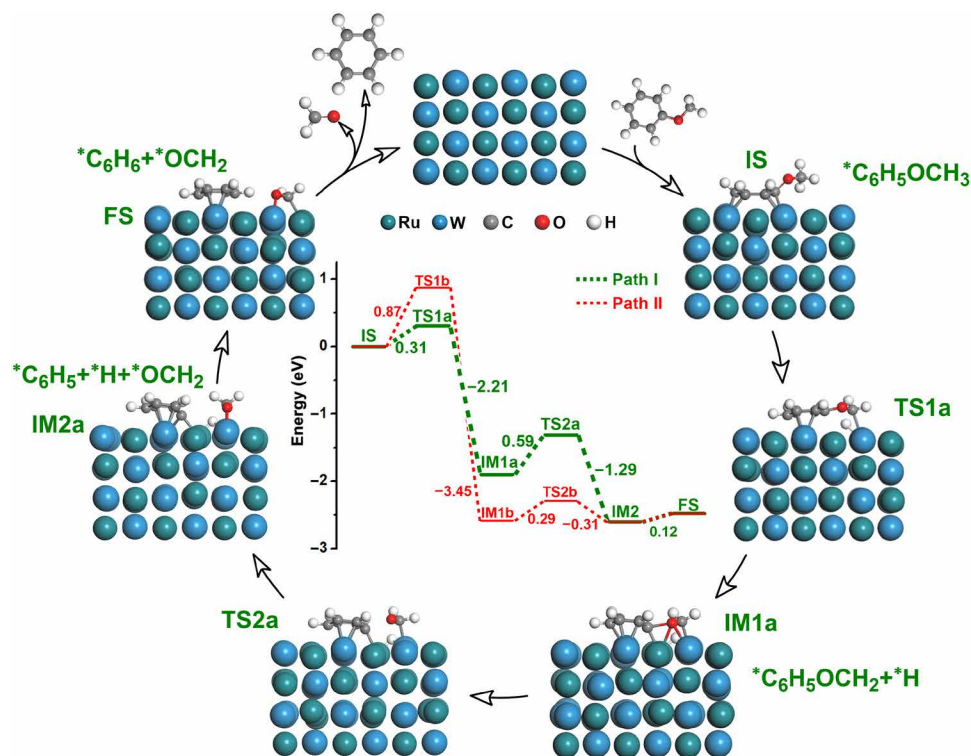

Fig. 3. Proposed mechanism for SSH reaction of anisole on RuW/SiO$_2$ catalyst. The inset shows the calculated profiles in electron volts. DFT optimized geometries of the structures of the initial state (IS) of anisole, final state (FS) of products, intermediates (IM), and transition states (TS) of the key elementary steps are shown in the reaction cycle (side view). The reaction cycle corresponds to the energy profile of path I, which is shown by the green dashed lines in the inset. The red dashed lines present the energy profile of path II specifically shown in fig. S5A.

replaced by CH_3 partially or completely (table S3, entries 2 to 5). It can be found that, without exogenous reductant, the reaction of phenol did not occur, whereas anisole could be singly transformed into benzene (table S3, entries 1 and 2), indicating that aliphatic H could be the reductant for the cleavage of the C_{Ar}—O bond. The yields of benzene decreased (table S3, entries 3 to 5) when more hydrogen in the methoxy group is replaced by CH_3. In particular, the yield of benzene approached zero when all the hydrogen atoms were replaced (table S3, entry 5). The results further indicate that the aliphatic H in methoxy group was the hydrogen source for the SSH reaction, and the original aliphatic C—O (C_{Al}—O) bond was transformed into the C_{Al}=O bond (table S3, entry 4). By comparison, with exogenous hydrogen in the catalytic system, the C_{Ar}—O bond was cleaved with a direct hydrogenolysis mechanism, and methanol was generated (table S3, entry 6) (*46*). However, under the same H_2 pressure, the hydrogenolysis of C_{Ar}—O bond in phenol was evidently more difficult than that in anisole (table S3, entries 6 and 7), confirming that the bond dissociation energy of the phenolic C_{Ar}—OH bond is higher than that of the ether C_{Ar}—OCH_3 bond (*47*). Consequently, the SSH reaction should be the coupling of effective activation of the C_{Al}—H bond and the highly efficient hydrogenolysis of the C_{Ar}—O bond, rather than the path with phenol as the intermediate.

As shown in the above path, the Ru and W atoms in the RuW catalyst demonstrated excellent synergy for the SSH reaction of anisole to benzene (fig. S5B). It is the synergism that confers the catalyst with outstanding activation of the C_{Al}—H bond in the methoxy group of anisole to support the hydrogenolysis of the C_{Ar}—O bond without exogenous reductant, which has also been confirmed by the unworkable SSH route over the monometallic Ru and W catalysts (Table 1, entries 2 and 17). Thus, with optimized Ru and W contents, the RuW/SiO_2 catalyst could have superior performance for the SSH reaction, affording full conversion of anisole to benzene at 175°C in 5.0 hours (fig. S7, A to D) with extremely high selectivity. Meanwhile, the RuW/SiO_2 catalyst exhibited excellent stability in the reaction, which was confirmed by reusing the catalyst (fig. S7E) and characterizations of the catalyst before and after the reaction by XRD (fig. S7F) and TEM techniques (fig. S7, G and H).

We also studied the SSH reaction of aromatic ether molecules with more methoxy or other functional groups over the RuW/SiO_2 catalyst. Figure 4 gives the optimized reaction conditions and the yields of corresponding desired aromatic products for various substrates. Dimethoxybenzenes (Fig. 4, conditions A1) could be converted to benzene, and their yields were >99.9%. Upon complete conversion of trimethoxylbenzene (Fig. 4, conditions A2), SSH chemistry produced 99.0% yield of benzene. 4-Methylanisole (Fig. 4, conditions B1) and 3,5-dimethoxytoluene (Fig. 4, conditions B2) could be transformed into toluene with a yield of >99.9%. In addition, the catalytic system could also efficiently catalyze the SSH reactions of methyleugenol (Fig. 4, conditions C1) and asarone (Fig. 4, conditions C2), which are allyl and multiple methoxyl group–substituted benzene derivatives to propylbenzene, and the yields could reach above 99.0%. It could be found that the double bond in the allyl group was saturated in the meantime, and the hydrogen was also derived from the methoxy groups. The generation of corresponding single arenes suggested the versatility of this methodology. To further study the catalytic performance of the SSH strategy, lignin-derived phenolic monomers, such as 2-methoxy-4-propylphenol (Fig. 4, conditions D1) and 2,6-dimethoxy-4-propylphenol (Fig. 4, conditions D2), were also used as the aromatic

ether model compounds with phenolic OH group (*25*, *28*). Both of them could be converted with propylbenzene as the single product, indicating that the SSH strategy could be applicable to the aromatic ethers with phenolic OH, and the effect of the electronegativity derived from the adjacent hydroxyl group on the reaction was not considerable.

We also studied the more challenging transformation of the kraft lignin (table S4), which is abundant in methoxylated phenylpropane structures with high molecular weight (*5*, *13*, *28*). The kraft lignin and the recovered residual solid were characterized by two-dimensional (2D) heteronuclear single-quantum coherence (HSQC) NMR techniques, and the spectra are shown in fig. S8. Taking into account that the reactivity of the methoxy group and β-aryl ether linkages (β-O-4) in lignin is the aim of the present work, the kraft lignin with less unresolved or unassigned signals was selected and used (*28*, *48*). It can be found that arenes were the main products from the transformation of the lignin (fig. S9A), and the product was dominated by propylbenzene with a yield of 8.5% (Fig. 5). In addition, benzene, toluene, and ethylbenzene were also produced with yields of 1.2, 0.6, and 0.9%, respectively. For comparison, the reaction of the kraft lignin was also performed without the RuW/SiO_2 catalyst under the same conditions, which could not yield the low–molecular weight products (fig. S9B).

As displayed in fig. S8, the signals of the methoxy group [at 56.0/3.70 parts per million (ppm), colored with yellow] and β-aryl ether linkage with phenylpropane structure (at 71.0/4.70, 83.5/4.30, and 60.0/3.40 ppm, colored with blue) in the side-chain region (*25*) decreased markedly after the reaction, suggesting the consumption of the methoxy group and β-aryl ether linkages to propylbenzene over the RuW/SiO_2 catalyst. In addition, the side-chain signals for resinol and phenylcoumaran also disappeared, which was probably due to the condensation (or repolymerization) of the side-chain carbon atoms with the adjacent aromatic/oligomer C atoms (*28*, *29*). The transformation of lignin always involves different reactions because of its complex structure (*13*, *25*), but the SSH reaction in this work is the crucial reaction in the lignin transformation. Under such catalytic strategy, the etheric and phenolic C_{Ar}—O bonds were cleaved efficiently, and arenes were generated. The detailed reaction mechanism needs to be studied further.

DISCUSSION

In summary, we developed an SSH strategy for the transformation of aromatic ethers into arenes. The RuW alloy catalyst in this work can catalyze the SSH reaction efficiently because it can abstract the hydrogen from the activated C_{Al}—H bond within the ethers and cleave the C_{Ar}—O bond via hydrogenolysis efficiently. The experimental results and DFT calculations confirmed that the neighboring Ru and W species in the RuW catalyst worked synergistically to accelerate the SSH reaction. The unique feature of SSH strategy is that exogenous hydrogen or other reductant is not required and hydrogenation of the aromatic ring could be avoided completely. The present SSH strategy also features simple operation conditions and is versatile for a wide range of aromatic ethers, such as ethers containing different functional groups, and lignin. For the reaction of an aromatic ether, arene selectivity can reach >99.9% at full conversion. For the transformation of lignin, propylbenzene is the dominant product with a yield of 8.5%. This work opens an advanced approach for the transformation of the C_{Ar}—O bond. We believe that the hydrogen-free and highly efficient methodology has great application potential to produce arenes from renewable biomass
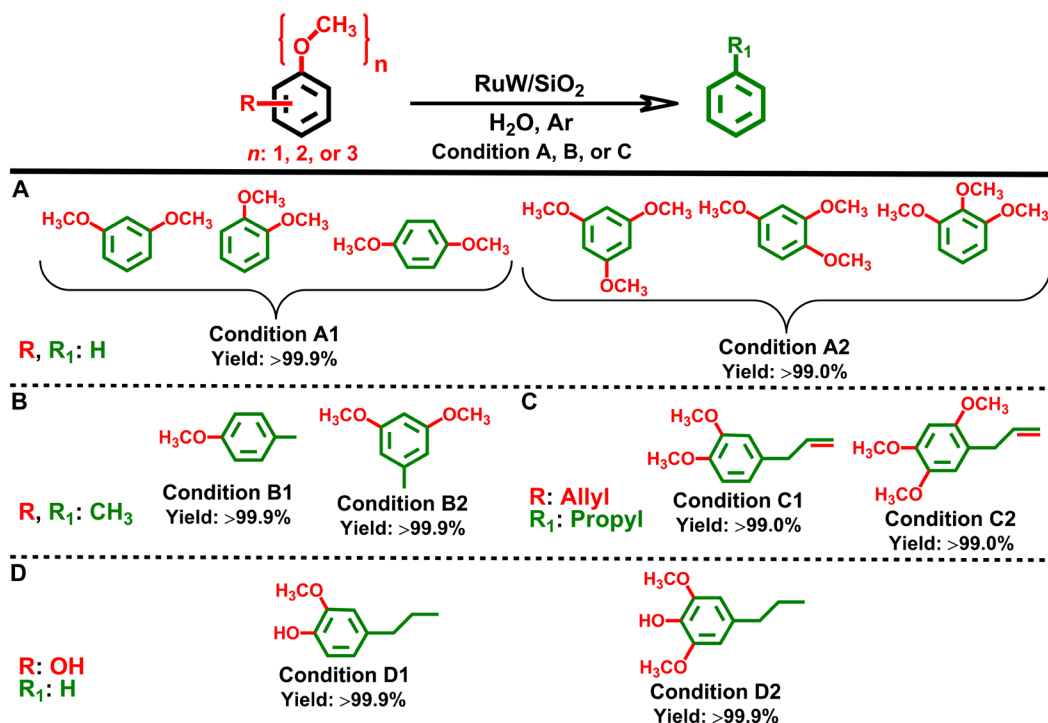
Fig. 4. Transformation of biomass-derived substrates to arenes. The general reaction scheme is shown at the top. The chemical structure colored with red is removed, and the chemical structure colored with green is the SSH product. Yields of products provided are at full conversion of substrates, as averages of three experiments conducted in parallel. Reaction conditions: Substrate (1.0 mmol), H_2O (5.0 ml), 0.5 MPa Ar, 800 rpm. (**A**) Condition A1: RuW/SiO_2 catalyst (100 mg, 3.5 wt % Ru, 20 wt % W), 195°C, 12 hours; condition A2: RuW/SiO_2 catalyst (110 mg, 4.0 wt % Ru, 30 wt % W), 210°C, 20 hours. (**B**) Condition B1: RuW/SiO_2 catalyst (90 mg, 3.5 wt % Ru, 20 wt % W), 180°C, 10 hours; condition B2: RuW/SiO_2 catalyst (110 mg, 3.5 wt % Ru, 20 wt % W), 200°C, 16 hours. (**C**) Condition C1: RuW/SiO_2 catalyst (130 mg, 4.0 wt % Ru, 30 wt % W), 230°C, 24 hours; condition C2: RuW/SiO_2 catalyst (140 mg, 4.0 wt % Ru, 30 wt % W), 240°C, 24 hours. (**D**) Condition D1: RuW/SiO_2 catalyst (110 mg, 3.5 wt % Ru, 20 wt % W), 210°C, 14 hours; condition D2: RuW/SiO_2 catalyst (120 mg, 3.5 wt % Ru, 20 wt % W), 220°C, 18 hours.
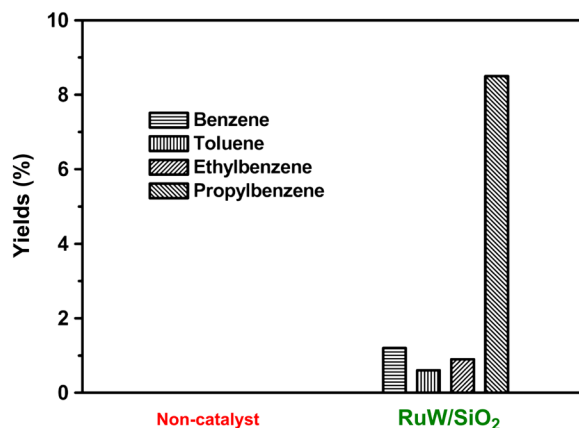

Fig. 5. Transformation of kraft lignin to arenes over RuW/SiO_2 catalysts. Reaction conditions: kraft lignin (0.5 g), RuW/SiO_2 catalyst (0.2 g, 5.0 wt % Ru, 40 wt % W), water (7.0 ml), 0.5 MPa Ar, 280°C, 24 hours, 800 rpm.

resources, and the scientific discovery is instructive for the exploration of some other new reactions.

MATERIALS AND METHODS
Materials
Anisole (99.0%), phenetole (98.0%), cyclohexanol (99.0%), biphenyl (99.0%), phenol (99.0%), benzene (99.0%), 4-methylanisole (99%),

4-allylanisole (98.0%), 3,5-dimethoxytoluene (98.0%), 1,3,5-trimethoxybenzene (99%), 1,2,4-trimethoxybenzene (98%), 1,2,3-trimethoxybenzene (98+%), *n*-propylbenzene (98.0%), ruthenium chloride hydrate (99.9%), palladium nitrate hydrate (99.8%), chloroplatinic acid hexahydrate (99.9%), ruthenium (IV) oxide (99.9%), tungsten (VI) oxide (99.9%), amorphous silicon oxide, formaldehyde (37%), *tert*-butanol (99.5%), isopropyl alcohol (99.5%), and tetrahydrofuran (99.8%) were purchased from Alfa Aesar. *tert*-Butyl phenyl ether (98.0%) was obtained from Adamas Reagent Co. Ltd. Isopropoxybenzene (97.0%) and asarone (98+%) were purchased from Ark Pharm. 1,2-Dimethoxybenzene (99%), 1,3-dimethoxybenzene (99%), 1,4-dimethoxybenzene (99%), and methoxycyclohexane (98%) were provided by TCI (Shanghai) Development Co. Ltd. 4-Allyl-1,2-dimethoxybenzene (99.0%), 2-methoxy-4-propylphenol (99%), and kraft lignin were purchased from Sigma-Aldrich Inc. Acetaldehyde (99.5%) and D_2O [100.0 atomic % (at %) D] were purchased from Acros Organics. 2,6-Dimethoxy-4-propylphenol (95%) was purchased from J&K Scientific Ltd. Ammonium metatungstate (AMT) hydrate (99.9+% W) was provided by Strem Chemicals. Methyl sulfoxide-d6 [D, 99.9%, 0.03% (v/v) tetramethylsilane (TMS)] was purchased from Cambridge Isotope Laboratories Inc. Toluene (99.5%) and ethylbenzene (98.5%) were obtained from Sinopharm Chemical Reagent Co. Ltd. Anisole-(methyl-d3) (99 at % D) was obtained from Beijing InnoChem Science & Technology Co. Ltd. Hydrochloric acid (37% in water), methanol (99.9%), ethanol (99.9%), ethyl acetate (99.5%), dichloromethane (99.5%), cyclohexanone (99.5%), cyclohexane (99.5%), acetone (99.5%), and *n*-hexane (95.0%) were obtained from the

Beijing Chemical Company. Nitrogen (>99.99%), argon (>99.99%), hydrogen/argon (H_2 10%, 99.99%), and hydrogen (>99.99%) were provided by Beijing Analytic Instrument Company.

Catalyst preparation

Supported RuW/SiO_2 catalysts were prepared by commonly used wet impregnation method. In a typical preparation, amorphous SiO_2 was dried at 120°C overnight before the impregnation. AMT (1.23 g) and $RuCl_3·xH_2O$] (0.39 g) were dissolved in 10 ml of deionized water. Then, the precursor solution containing AMT and Ru^{3+} ion was successively added dropwise to 60 ml of deionized water with 2 g of amorphous SiO_2 at room temperature. The obtained mixture was vigorously stirred for 48 hours, evaporated, and dried at 473 K for 16 hours in an oven. The as-prepared samples were reduced in a continuous 10% H_2/Ar flow, from room temperature to 400°C at 5°C min^{-1} and then to 900°C at 1°C min^{-1}, and maintained at 900°C for 1 hour. After being cooled to room temperature under Ar atmosphere, the reduced catalysts were exposed to 1% O_2/Ar atmosphere for 1 hour to form a passivation layer to prohibit against bulk oxidation before exposure to air. The passivated catalysts were kept under an inert atmosphere before testing and characterizations, and denoted as RuW/SiO_2. For comparison, supported Ru/SiO_2, W/SiO_2, and other catalysts were prepared by the same procedures for preparing the RuW/SiO_2 catalyst.

Catalyst characterization

The catalysts were characterized by N_2 adsorption-desorption, XRD, XPS, XAFS, TEM, HRTEM, and inductively coupled plasma atomic emission spectroscopy (ICP-AES) techniques. N_2 adsorption-desorption of the samples was measured using a Micromeritics TriStar II 3020 system at liquid nitrogen temperature. The sample was degassed at 300°C under vacuum for 24 hours before analysis. The specific surface areas were calculated by using the Brunauer-Emmett-Teller model. The pore size distribution of the sample was calculated using the Barrett-Joyner-Halenda pore size model. XRD measurements were conducted on an x-ray diffractometer (D/MAX-RC, Japan) operated at 40 kV and 200 mA with Cu Kα (λ = 0.154 nm) radiation. Rietveld refinements were performed applying the TOPAS program (49) for the measured XRD profile of the RuW/SiO_2 catalyst. The XPS measurements were carried out on an ESCALAB 220i-XL spectrometer at a pressure of ~3×10^{-9} mbar (1 mbar = 100 Pa) using Al Kα as the excitation source (hv = 1486.6 eV) and operated at 15 kV and 20 mA. The XAFS spectra (Cu K-edge) were collected at 1W1B station in Beijing Synchrotron Radiation Facility (BSRF). The storage rings of BSRF were operated at 2.5 GeV with a maximum current of 250 mA. Using Si (111) double-crystal monochromator, the data collection was carried out in transmission mode using ionization chamber. All spectra were collected in ambient conditions. The acquired EXAFS data were processed according to the standard procedures using the ATHENA module implemented in the IFEFFIT software packages. The k3-weighted EXAFS spectra were obtained by subtracting the post-edge background from the overall absorption and then normalizing with respect to the edge-jump step. Subsequently, k3-weighted χ(k) data of Cu K-edge were Fourier-transformed to real (R) space using a hanning windows (dk = 1.0 $Å^{-1}$) to separate the EXAFS contributions from different coordination shells. To obtain the quantitative structural parameters around central atoms, least-squares curve parameter fitting was performed using the ARTEMIS module of IFEFFIT soft-

ware packages (50). TEM and HRTEM images were obtained using a JEOL-2011F electron microscope operating at 200 kV. Before measurement, the catalyst was ground, suspended in ethanol, and dispersed by ultrasonic treatment. The obtained dispersion was transferred to a copper grid–supported carbon film. The contents of supported metals on the catalysts were determined by ICP.

Catalytic performance

The reaction was carried out in a Teflon-lined stainless steel reactor of 20 ml with a magnetic stirrer. In a typical experiment, a suitable amount of reactant, catalyst, and solvent were loaded into the reactor. The reactor was sealed, purged with Ar gas three times to remove the air at room temperature, and subsequently charged with 0.5 MPa desired gas. Then, the reactor was placed in a furnace at the reaction temperature, and the reactor reached the desired reaction temperature within 20 min. After that, the stirrer was started with a stirring speed of 800 rpm, and the reaction time was recorded. After the reaction, the reactor was placed in ice water and the gas was released passing through ethyl acetate and then collected in a gas bag that was purged with Ar for five times. The gaseous sample was analyzed using a GC (Agilent 4890D) equipped with a thermal conductivity detector (TCD) detector and a packed column (carbon molecular sieve TDX-01, 1 m in length and 3 mm in diameter) using argon as the carrier gas. The liquid reaction mixture in the reactor was transferred into a centrifuge tube. Then, the reactor was washed with the ethyl acetate used for the gas filtration, which was finally combined with the reaction mixture. After centrifugation, the catalyst was separated from the reaction mixture. The quantitative analysis of the liquid products in the organic phase was conducted using a GC (Agilent 6820) equipped with a flame ionization detector and HP-5ms/HP-INNOWax capillary columns (0.25 mm in diameter, 30 m in length). Identification of the products and reactant was performed using a gas chromatography–mass spectrometry system [Agilent 5977A, HP-5ms capillary column (0.25 mm in diameter and 30 m in length)] as well as by comparing the retention time to respective standards in GC traces. Biphenyl was used as the internal standard with a quantity of 40 mg to determine the conversions of substrates, selectivities, and yields of the products. Identification of the products in the aqueous phase was conducted by ^{1}H NMR analysis on a Bruker Avance III 400 HD with D_2O as the solvent. The carbon balance for the transformation of the aromatic ethers was composed of $C_{aromatics}$ and $C_{methoxyl}$ balances, which were given relative to the aromatic and methoxyl-derived products, respectively (51). The $C_{aromatics}$ and $C_{methoxyl}$ balances for the transformation of small-molecule aromatic ethers were better than 99 and 98%, respectively. Mass balance for the lignin transformation was calculated using Eq. 1 (52). After the reaction, solid and liquid were separated by centrifugation, and the mass of the solid recovered was nearly the same as that of the catalyst charged. For the lignin transformation, internal standard (biphenyl for the organic phase) was used to determine the yields of the detectable products. After the recovery of the catalyst, the liquid reaction mixtures were subjected to the rotavap to remove the solvents and the volatile products. Then, the recovered residual solid was dried in a vacuum oven at 50°C overnight. For the transformation of lignin catalyzed by RuW/SiO_2, the mass balance was 90 ± 5%. The structure of the kraft lignin and the recovered residual solid were analyzed by 2D HSQC NMR spectroscopy (Bruker Avance III 600 HD), as described from other researchers (53). Organic elemental analysis (C, H, N, and S) was carried out using the

classical total oxidation method on Flash EA 1112 with an Elementar system model (vario MICRO cube). The contents of inorganic elements in the lignin were determined by ICP-AES (Vista-MPX).

$$\text{Mass balance} = \frac{\text{Detectable products + residual solid}}{\text{Lignin charged}} \times 100\% \quad (1)$$

Recycling of the catalyst

The reusability of the RuW/SiO$_2$ catalyst was tested for the anisole transformation in water. After the reaction, the reaction mixture was centrifuged and analyzed using a GC. The solid RuW/SiO$_2$ catalyst was recovered and successively washed with ethanol (5 × 10 ml) and water (5 × 10 ml). Then, the RuW/SiO$_2$ catalyst was reused directly for the next run.

Computational methodology

DFT calculation was carried out using the Vienna Ab initio Simulation Package (VASP) (54). The spin-polarized projector augmented wave method (55), Perdew-Burke-Ernzerhof (PBE) (56), and electron exchange-correlation function of the generalized gradient approximation (57) were used. The kinetic energy cutoff for the wave function expanded in the plane-wave basis was set to 400 eV. To optimize the structures, the calculation was performed until the maximum force upon each relaxed atom was less than 0.05 eV/Å. The vacuum height was set to 15 Å to eliminate the interaction between neighboring slabs. The spin-polarized calculations were carried out with the DFT (PBE)–D3 (Becke-Jonson) scheme (58) as implemented in VASP. Default values of the dispersion coefficient (C$_6$) and the vdW radii (R$_0$) parameters given by Grimme et al. (58) were used.

The adsorption energy (E$_{ads}$) was calculated as follows:

$$E_{ads} = -(E_{total} - E_{substrate} - E_{gas\text{-}phase\ adsorbate})$$

where E$_{total}$ is the calculated total energy of the adsorption system, E$_{substrate}$ is the energy of the clean substrate, and E$_{gas\text{-}phase\ adsorbate}$ is the energy of the gas-phase molecule.

To study the mechanism of anisole dissociation on RuW surfaces, we used the following models: A 3 × 3 surface cell was used to construct a four-layer RuW (110) slab, and the top three layers of the RuW (110) slab were allowed to relax. The Brillouin zone integration was performed along with a 2 × 2 × 1 Monkhorst-Pack grid for the different surface slabs.

SUPPLEMENTARY MATERIALS

Supplementary material for this article is available at http://advances.sciencemag.org/cgi/content/full/5/11/eaax6839/DC1

Fig. S1. Nitrogen adsorption-desorption isotherm and the pore size distribution of the SiO$_2$ support.
Fig. S2. The analyses of the liquid and gaseous product obtained from the transformation of anisole over the RuW/SiO$_2$ catalyst.
Fig. S3. EDS elemental mapping analysis of the RuW/SiO$_2$ catalyst.
Fig. S4. XANES and FT-EXAFS spectra of RuW/SiO$_2$ catalyst.
Fig. S5. Proposed path II mechanism for SSH reaction and DFT optimized geometries in the proposed mechanism.
Fig. S6. Identification of formaldehyde and origination of the negatively charged hydrogen in hydrogenolysis.
Fig. S7. Optimization of reaction conditions over RuW/SiO$_2$ catalyst, recyclability and stability of RuW/SiO$_2$ catalyst.
Fig. S8. 2D HSQC NMR spectra of the kraft lignin before and after the transformation with RuW/SiO$_2$ catalyst.
Fig. S9. GC trace of liquid products generated from the transformation of the kraft lignin.
Table S1. Results for the transformation of anisole in different solvent systems.
Table S2. Structure parameters of the RuW/SiO$_2$ catalyst extracted from the EXAFS fitting.
Table S3. Results for the transformation of substrates over the RuW/SiO$_2$ catalyst.
Table S4. Elemental analysis of the kraft lignin sample.
Reference (59)

REFERENCES AND NOTES

1. A. D. Sutton, F. D. Waldie, R. L. Wu, M. Schlaf, L. A. Silks III, J. C. Gordon, The hydrodeoxygenation of bioderived furans into alkanes. *Nat. Chem.* **5**, 428–432 (2013).
2. M. Y. He, Y. H. Sun, B. X. Han, Green carbon science: Scientific basis for integrating carbon resource processing, utilization, and recycling. *Angew. Chem. Int. Ed.* **52**, 9620–9633 (2013).
3. Q. Meng, M. Hou, H. Liu, J. Song, B. Han, Synthesis of ketones from biomass-derived feedstock. *Nat. Commun.* **8**, 14190 (2017).
4. C. O. Tuck, E. Pérez, I. T. Horváth, R. A. Sheldon, M. Poliakoff, Valorization of biomass: Deriving more value from waste. *Science* **337**, 695–699 (2012).
5. A. J. Ragauskas, G. T. Beckham, M. J. Biddy, R. Chandra, F. Chen, M. F. Davis, B. H. Davison, R. A. Dixon, P. Gilna, M. Keller, P. Langan, A. K. Naskar, J. N. Saddler, T. J. Tschaplinski, G. A. Tuskan, C. E. Wyman, Lignin valorization: Improving lignin processing in the biorefinery. *Science* **344**, 709–719 (2014).
6. W. Deng, Y. Wang, S. Zhang, K. M. Gupta, M. J. Hulsey, H. Asakura, L. Liu, Y. Han, E. M. Karp, G. T. Beckham, P. J. Dyson, J. Jiang, T. Tanaka, Y. Wang, N. Yan, Catalytic amino acid production from biomass-derived intermediates. *Proc. Natl. Acad. Sci. U.S.A.* **115**, 5093–5098 (2018).
7. K. Caballero-Gallardo, J. Olivero-Verbel, E. E. Stashenko, Repellent activity of essential oils and some of their individual constituents against *Tribolium castaneum* herbst. *J. Agric. Food Chem.* **59**, 1690–1696 (2011).
8. S. Lv, Y. Wu, C. Li, Y. Xu, L. Liu, Q. Meng, Comparative analysis of Pu-erh and Fuzhuan teas by fully automatic headspace solid-phase microextraction coupled with gas chromatography–mass spectrometry and chemometric methods. *J. Agric. Food Chem.* **62**, 1810–1818 (2014).
9. L. M. Seitz, M. S. Ram, Volatile methoxybenzene compounds in grains with off-odors. *J. Agric. Food Chem.* **48**, 4279–4289 (2000).
10. L. Du, C. Wang, J. Li, D. Xiao, C. Li, Y. Xu, Optimization of headspace solid-phase microextraction coupled with gas chromatography-mass spectrometry for detecting methoxyphenolic compounds in pu-erh tea. *J. Agric. Food Chem.* **61**, 561–568 (2013).
11. R. G. Atkinson, Phenylpropenes: Occurrence, distribution, and biosynthesis in fruit. *J. Agric. Food Chem.* **66**, 2259–2272 (2018).
12. C.-P. Xiang, J.-X. Han, X.-C. Li, Y.-H. Li, Y. Zhang, L. Chen, Y. Qu, C.-Y. Hao, H.-Z. Li, C.-R. Yang, S.-J. Zhao, M. Xu, Chemical composition and acetylcholinesterase inhibitory activity of essential oils from piper species. *J. Agric. Food Chem.* **65**, 3702–3710 (2017).
13. J. Zakzeski, P. C. A. Bruijnincx, A. L. Jongerius, B. M. Weckhuysen, The catalytic valorization of lignin for the production of renewable chemicals. *Chem. Rev.* **110**, 3552–3599 (2010).
14. S. H. Morejudo, R. Zanon, S. Escolástico, I. Yuste-Tirados, H. Malerød-Fjeld, P. K. Vestre, W. G. Coors, A. Martínez, T. Norby, J. M. Serra, C. Kjølseth, Direct conversion of methane to aromatics in a catalytic co-ionic membrane reactor. *Science* **353**, 563–566 (2016).
15. P. A. Jacobs, M. Dusselier, B. F. Sels, Will zeolite-based catalysis be as relevant in future biorefineries as in crude oil refineries? *Angew. Chem. Int. Ed.* **53**, 8621–8626 (2014).
16. C. Li, X. Zhao, A. Wang, G. W. Huber, T. Zhang, Catalytic transformation of lignin for the production of chemicals and fuels. *Chem. Rev.* **115**, 11559–11624 (2015).
17. T. D. Matson, K. Barta, A. V. Iretskii, P. C. Ford, One-pot catalytic conversion of cellulose and of woody biomass solids to liquid fuels. *J. Am. Chem. Soc.* **133**, 14090–14097 (2011).
18. J. He, C. Zhao, J. A. Lercher, Ni-catalyzed cleavage of aryl ethers in the aqueous phase. *J. Am. Chem. Soc.* **134**, 20768–20775 (2012).
19. F. Gao, J. D. Webb, J. F. Hartwig, Chemo- and regioselective hydrogenolysis of diaryl ether C–O bonds by a robust heterogeneous Ni/C Catalyst: Applications to the cleavage of complex lignin-related fragments. *Angew. Chem. Int. Ed.* **55**, 1474–1478 (2016).
20. R. Rinaldi, R. Jastrzebski, M. T. Clough, J. Ralph, M. Kennema, P. C. A. Bruijnincx, B. M. Weckhuysen, Paving the way for lignin valorisation: Recent advances in bioengineering, biorefining and catalysis. *Angew. Chem. Int. Ed.* **55**, 8164–8215 (2016).
21. W. Lan, J. B. de Bueren, J. S. Luterbacher, Highly selective oxidation and depolymerization of α,γ-diol-protected lignin. *Angew. Chem. Int. Ed.* **58**, 2649–2654 (2019).
22. W. Deng, H. Zhang, X. Wu, R. Li, Q. Zhang, Y. Wang, Oxidative conversion of lignin and lignin model compounds catalyzed by CeO$_2$-supported Pd nanoparticles. *Green Chem.* **17**, 5009–5018 (2015).
23. A. Rahimi, A. Ulbrich, J. J. Coon, S. S. Stahl, Formic-acid-induced depolymerization of oxidized lignin to aromatics. *Nature* **515**, 249–252 (2014).

24. P. J. Deuss, M. Scott, F. Tran, N. J. Westwood, J. G. de Vries, K. Barta, Aromatic monomers by in situ conversion of reactive intermediates in the acid-catalyzed depolymerization of lignin. *J. Am. Chem. Soc.* **137**, 7456–7467 (2015).

25. Z. H. Sun, B. Fridrich, A. de Santi, S. Elangovan, K. Barta, Bright side of lignin depolymerization: Toward new platform chemicals. *Chem. Rev.* **118**, 614–678 (2018).

26. H. Q. Zeng, D. W. Cao, Z. H. Qiu, C.-J. Li, Palladium-catalyzed formal cross-coupling of diaryl ethers with amines: Slicing the 4-O-5 linkage in lignin models. *Angew. Chem. Int. Ed.* **57**, 3752–3757 (2018).

27. X. J. Wu, X. T. Fan, S. J. Xie, J. C. Lin, J. Cheng, Q. H. Zhang, L. Y. Chen, Y. Wang, Solar energy-driven lignin-first approach to full utilization of lignocellulosic biomass under mild conditions. *Nat. Catal.* **1**, 772–780 (2018).

28. L. Shuai, M. T. Amiri, Y. M. Questell-Santiago, F. Héroguel, Y. Li, H. Kim, R. Meilan, C. Chapple, J. Ralph, J. S. Luterbacher, Formaldehyde stabilization facilitates lignin monomer production during biomass depolymerization. *Science* **354**, 329–333 (2016).

29. Y. Li, L. Shuai, H. Kim, A. H. Motagamwala, J. K. Mobley, F. Yue, Y. Tobimatsu, D. Havkin-Frenkel, F. Chen, R. A. Dixon, J. S. Luterbacher, J. A. Dumesic, J. Ralph, An "ideal lignin" facilitates full biomass utilization. *Sci. Adv.* **4**, eaau2968 (2018).

30. S.-i. Niwa, M. Eswaramoorthy, J. Nair, A. Raj, N. Itoh, H. Shoji, T. Namba, F. Mizukami, A one-step conversion of benzene to phenol with a palladium membrane. *Science* **295**, 105–107 (2002).

31. E. L. Kunkes, D. A. Simonetti, R. M. West, J. C. Serrano-Ruiz, C. A. Gärtner, J. A. Dumesic, Catalytic conversion of biomass to monofunctional hydrocarbons and targeted liquid-fuel classes. *Science* **322**, 417–421 (2008).

32. Y. Shao, Q. Xia, L. Dong, X. Liu, X. Han, S. F. Parker, Y. Q. Cheng, L. L. Daemen, A. J. Ramirez-Cuesta, S. Yang, Y. Wang, Selective production of arenes via direct lignin upgrading over a niobium-based catalyst. *Nat. Commun.* **8**, 16104 (2017).

33. W.-S. Lee, Z. Wang, R. J. Wu, A. Bhan, Selective vapor-phase hydrodeoxygenation of anisole to benzene on molybdenum carbide catalysts. *J. Catal.* **319**, 44–53 (2014).

34. J. Cornella, E. Gómez-Bengoa, R. Martin, Combined experimental and theoretical study on the reductive cleavage of Inert C-O bonds with silanes: Ruling out a classical Ni(0)/Ni(II) catalytic couple and evidence for Ni(I) intermediates. *J. Am. Chem. Soc.* **135**, 1997–2009 (2013).

35. K. D. Nguyen, B. Y. Park, T. Luong, H. Sato, V. J. Garza, M. J. Krische, Metal-catalyzed reductive coupling of olefin-derived nucleophiles: Reinventing carbonyl addition. *Science* **354**, ah5133 (2016).

36. Q. Xia, Z. Chen, Y. Shao, X. Gong, H. Wang, X. Liu, S. F. Parker, X. Han, S. Yang, Y. Wang, Direct hydrodeoxygenation of raw woody biomass into liquid alkanes. *Nat. Commun.* **7**, 11162 (2016).

37. X. Xu, Y. Li, Y. Gong, P. Zhang, H. Li, Y. Wang, Synthesis of palladium nanoparticles supported on mesoporous n-doped carbon and their catalytic ability for biofuel upgrade. *J. Am. Chem. Soc.* **134**, 16987–16990 (2012).

38. S. García-Fernández, I. Gandarias, J. Requies, M. B. Güemez, S. Bennici, A. Auroux, P. L. Arias, New approaches to the Pt/WOx/Al₂O₃ catalytic system behavior for the selective glycerol hydrogenolysis to 1, 3-propanediol. *J. Catal.* **323**, 65–75 (2015).

39. J. W. Ribblett, W. E. Sinclair, D. R. Borst, J. T. Yi, D. W. Pratt, High resolution electronic spectra of anisole and anisole–water in the gas phase: Hydrogen bond switching in the S₁ state. *J. Phys. Chem. A* **110**, 1478–1483 (2006).

40. J. S. Brown, J. P. Hallett, D. Bush, C. A. Eckert, Liquid–liquid equilibria for binary mixtures of water + acetophenone, + 1-octanol, + anisole, and + toluene from 370 K to 550 K. *J. Chem. Eng. Data* **45**, 846–850 (2000).

41. L. Huang, X. Zhang, Q. Wang, Y. Han, Y. Fang, S. Dong, Shape-control of Pt–Ru nanocrystals: Tuning surface structure for enhanced electrocatalytic methanol oxidation. *J. Am. Chem. Soc.* **140**, 1142–1147 (2018).

42. B. Sieve, X. Z. Chen, R. Henning, P. Brazis, C. R. Kannewurf, J. A. Cowen, A. J. Schultz, M. G. Kanatzidis, Cubic aluminum silicides RE₈Ru₁₂Al₄₉Si₉ (AlₓSi₁₂₋ₓ) (RE = Pr, Sm) from liquid aluminum. Empty (Si, Al)₁₂ cuboctahedral clusters and assignment of the Al/Si distribution with neutron diffraction. *J. Am. Chem. Soc.* **123**, 7040–7047 (2001).

43. S. Ji, Y. Chen, Q. Fu, Y. Chen, J. Dong, W. Chen, Z. Li, Y. Wang, L. Gu, W. He, C. Chen, Q. Peng, Y. Huang, X. Duan, D. Wang, C. Draxl, Y. Li, Confined pyrolysis within metal–organic frameworks to form uniform Ru₃ clusters for efficient oxidation of alcohols. *J. Am. Chem. Soc.* **139**, 9795–9798 (2017).

44. F. Yang, X. Wang, D. Zhang, J. Yang, D. Luo, Z. Xu, J. Wei, J.-Q. Wang, Z. Xu, F. Peng, X. Li, R. Li, Y. Li, M. Li, X. Bai, F. Ding, Y. Li, Chirality-specific growth of single-walled carbon nanotubes on solid alloy catalysts. *Nature* **510**, 522–524 (2014).

45. D. Townsend, S. A. Lahankar, S. K. Lee, S. D. Chambreau, A. G. Suits, X. Zhang, J. Rheinecker, L. B. Harding, J. M. Bowman, The roaming atom: Straying from the reaction path in formaldehyde decomposition. *Science* **306**, 1158–1161 (2004).

46. Y.-B. Huang, L. Yan, M.-Y. Chen, Q.-X. Guo, Y. Fu, Selective hydrogenolysis of phenols and phenyl ethers to arenes through direct C–O cleavage over ruthenium–tungsten bifunctional catalysts. *Green Chem.* **17**, 3010–3017 (2015).

47. Q. Tan, G. H. Wang, A. Long, A. Dinse, C. Buda, J. Shabaker, D. E. Resasco, Mechanistic analysis of the role of metal oxophilicity in the hydrodeoxygenation of anisole. *J. Catal.* **347**, 102–115 (2017).

48. C. S. Lancefield, H. L. J. Wienk, R. Boelens, B. M. Weckhuysena, P. C. A. Bruijnincx, Identification of a diagnostic structural motif reveals a new reaction intermediate and condensation pathway in kraft lignin formation. *Chem. Sci.* **9**, 6348–6360 (2018).

49. M. Schrinner, M. Ballauff, Y. Talmon, Y. Kauffmann, J. Thun, M. Möller, J. Breu, Single nanocrystals of platinum prepared by partial dissolution of Au-Pt nanoalloys. *Science* **323**, 617–620 (2009).

50. B. Ravel, M. Newville, ATHENA, ARTEMIS, HEPHAESTUS: Data analysis for X-ray absorption spectroscopy using IFEFFIT. *J. Synchrotron Radiat.* **12**, 537–541 (2005).

51. Z. Cao, J. Engelhardt, M. Dierks, M. T. Clough, G.-H. Wang, E. Heracleous, A. Lappas, R. Rinaldi, F. Schüth, Catalysis meets nonthermal separation for the production of (Alkyl) phenols and hydrocarbons from pyrolysis oil. *Angew. Chem. Int. Ed.* **56**, 2334–2339 (2017).

52. A. K. Deepa, P. L. Dhepe, Lignin depolymerization into aromatic monomers over solid acid catalysts. *ACS Catal.* **5**, 365–379 (2015).

53. A. Rahimi, A. Azarpira, H. Kim, J. Ralph, S. S. Stahl, Chemoselective metal-free aerobic alcohol oxidation in lignin. *J. Am. Chem. Soc.* **135**, 6415–6418 (2013).

54. G. Kresse, J. Furthmuller, Efficient iterative schemes for *ab initio* total-energy calculations using a plane-wave basis set. *Phys. Rev. B* **54**, 11169–11186 (1996).

55. P. E. Blöchl, Projector augmented-wave method. *Phys. Rev. B* **50**, 17953–17979 (1994).

56. J. P. Perdew, K. Burke, M. Ernzerhof, Generalized gradient approximation made simple. *Phys. Rev. Lett.* **77**, 3865–3868 (1996).

57. M. P. Teter, M. C. Payne, D. C. Allan, Solution of Schrödinger's equation for large systems. *Phys. Rev. B* **40**, 12255–12263 (1989).

58. S. Grimme, J. Antony, S. Ehrlich, S. Krieg, A consistent and accurate *ab initio* parametrization of density functional dispersion correction (DFT-D) for the 94 elements H-Pu. *J. Chem. Phys.* **132**, 154104 (2010).

59. D. Mei, A. M. Karim, Y. Wang, On the reaction mechanism of acetaldehyde decomposition on Mo (110). *ACS Catal.* **2**, 468–478 (2012).

Citation: Q. Meng, J. Yan, H. Liu, C. Chen, S. Li, X. Shen, J. Song, L. Zheng, B. Han, Self-supported hydrogenolysis of aromatic ethers to arenes. *Sci. Adv.* **5**, eaax6839 (2019).